AIAA AVIATION Forum
June 15-19, 2020, VIRTUAL EVENT
AIAA AVIATION 2020 FORUM

10.2514/6.2020-2796

A Multi-Fidelity Approach to Predicting Rotor Aerodynamic Interactions

Orazio Pinti*, Assad A. Oberai †
University of Southern California, Los Angeles, CA, 90089

Robert J. Niemiec‡, Farhan Gandhi §
Center for Mobility with Vertical Lift, Rensselaer Polytechnic Institute, Troy, NY, 12180

Recent years have seen a huge interest in large electric multicopters for Urban Air Mobility, commercial package delivery, and military/law enforcement applications. This has lead to a growing interest in modeling the interactional aerodynamic effects of rotors operating in close proximity and their impact on performance. While CFD can be used to understand the detailed physics of multi-rotor interaction, in most cases it is too computationally demanding for performing optimization and uncertainty quantification studies over a range of parameters. On the other hand, lower-fidelity models approximate the underlying physics and are computationally inexpensive, however they are often inaccurate in predicting the desired fields of interest. With this in mind, in this study we present a multi-fidelity approach that inherits the computational efficiency of a low-fidelity model while retaining the accuracy of a high-fidelity method. This approach is based on using the low-fidelity model to span the entire space of parameters, using these results to identify the key parameter values to perform high-fidelity simulations, and then using these in a lifting procedure to determine multi-fidelity solutions at other parameter values. In this manuscript we apply this strategy to determine the disk plots of lift and drag for the two rotors of a multicopter as a function of the longitudinal and vertical distance between them. We note that this strategy can substantially improve upon the low-fidelity results.

I. Nomenclature

$\boldsymbol{\theta}$	=	point in the parameter space
d_x, d_y	=	longitudinal and vertical distance between rotors
$\boldsymbol{u}(\boldsymbol{\theta})$	=	vector of a simulation result – *snapshot* – with parameters given by $\boldsymbol{\theta}$
$\boldsymbol{u}^L$, $\boldsymbol{u}^H$	=	snapshots obtained with a low and high-fidelity model respectively
$\boldsymbol{U}^L$, $\boldsymbol{U}^H$	=	matrix whose columns are low or high-fidelity snapshots
$\boldsymbol{U}_n$	=	matrix with just n snapshots stored
$\hat{\boldsymbol{u}}$	=	approximation of the snapshot $\boldsymbol{u}$

II. Introduction

The last three years have seen a huge interest in large electric multicopters (eVTOL aircraft) for Urban Air Mobility (for example, in the Uber Elevate vision and the NASA UAM Grand Challenge), commercial package delivery, and military/law enforcement applications. The current batteries powering most of these multi-copters exhibit very low energy density relative to hydrocarbon fuels used by larger convectional VTOL aircraft. With this limitation, it is especially important to maximize eVTOL aircraft aerodynamic performance in order to realize practical payload capacity, endurance and range. A time efficient aerodynamics characterization of various multicopters design becomes thus very appealing. One area that requires particular attention is the understanding of the interactional aerodynamic

*PhD Student, pinti@usc.edu.
†Hughes Professor of Aerospace and Mechanical Engineering at USC, aoberai@usc.edu.
‡Lecturer, niemir2@rpi.edu, AIAA Member
§Rosalind and John J. Redfern Jr Chair in Engineering, Mechanical, Aerospace and Nuclear Engineering at RPI, gandhf@rpi.edu, AIAA Fellow

effects of rotors operating in close proximity and their impact on performance.

A number of recent studies have used Computational Fluid Dynamics (CFD) to simulate and understand the complex flows associated with interactional aerodynamics of rotors operating in close proximity. Researchers at the NASA Advanced Supercomputing Division have used CFD to simulate large and small-scale quadcopters in hover and forward flight. Yoon et al. [1] investigated the effects of rotor separation for an XV-15 derivative quadcopter in hover, and observed up to a 4% decrease in rotor efficiency for rotors in close proximity. At the smaller scale, Yoon et al. simulated the Straight Up Imaging (SUI) Endurance quad-copter in 10 m/s cruise [2] and reported a 28% thrust deficit on the aft rotors when compared to those rotors operating in isolation. Other work by Diaz and Yoon [3] found that vertical rotor separation via over/under mounting influenced rotor interaction on a quadcopter in cruise. Misiorowski, Gandhi and Oberai also used CFD to simulate quadcopters operating in cruise in the plus and cross configurations [4], and provided physical insights into the difference in interactional aerodynamics for the two configurations. CFD simulations of in-line large UAM scale rotors in cruise by Healy, Misiorowski and Gandhi [5] were used to systematically examine the effects of vertical and longitudinal rotor spacing on interactional aerodynamic effects.

While the CFD approach described above provides detailed physics of multi-rotor interaction, in most cases it is too computationally demanding for performing optimization and uncertainty quantification (UQ) studies over a range of parameters. This is because these studies require a large number (often in the order of 100-10,000) of simulations of the system at different configurations. Therefore, in these types of studies a lower-fidelity model, which is computationally inexpensive, is used. However, these types of models approximate the underlying physics, and that leads to inaccuracies in the predicted quantities of interest (QoIs). It is therefore useful to develop methods that combine the desirable characteristics of both high- and low-fidelity approaches. That is, they inherit the computational efficiency of the low-fidelity model, while retaining the accuracy of the high-fidelity one.

The multi-fidelity approach adopted in this paper was developed in [6], further analyzed in [7, 8], and applied to topology optimization under uncertainty in [9]. It comprises of the following steps:

1) Perform a large number of low-fidelity simulations to generate snapshots that span the Domain of Interest (DoI) in the parametric space.
2) Find the parameter values corresponding to the most important low-fidelity snapshots, and then express each of the remaining snapshots in the set in terms of these important ones.
3) Perform the high-fidelity simulation at the parameter values corresponding to the important snapshots to generate the corresponding high-fidelity snapshots.
4) Use the expansion coefficients computed in Step 2, but with the high-fidelity snapshots computed in Step 3, in order to determine the multi-fidelity approximation of the solution in the whole DoI.

We note that there are several methods to determine the important snapshots in Step 2 above [10]. These include the leverage sampling, a SVD-based method to solve the *column subset selection problem* (CSSP) [11, 12], a pivoted Cholesky decomposition [6, 7], or a pivoted QR decomposition [13–15]. In this work we utilize the QR decomposition, which has been observed to better perform [16, 17].

We apply the multi-fidelity approach to predict the behavior of the rotors of a dual-rotor multicopter in forward flight when the relative distance between them is varied. The parameters we consider are the longitudinal and vertical distance between the two rotors. The fields we are interested in predicting are the disk plots of lift and drag distribution for both the rotors. Using the disk plots we can compute the total thrust and torque for each rotor. For the high-fidelity model we use a CFD model of the system and for the low-fidelity model we use the RMAC model [18], which is based on a blade element approximation of the original model.

The format of the remainder of this manuscript is as follows. In Section III, we formulate the problem of interest by describing the high-fidelity and the low-fidelity models in more details and the strategy for combining them. We present numerical results in Section IV, and end with conclusions in Section V.

III. Problem Formulation

The case under investigation is of two rotors of a multicopter in forward flight. The two rotors are aligned with the forward velocity and the fields of interest are the disk plots of lift and drag. The relative position of the rotors can be described using the longitudinal and the vertical distance between them. These two quantities, denoted by d_x and d_y, define a two-dimensional parameter space, $\boldsymbol{\theta} = (d_x, d_y)$, for the system of interest. There is a one-to-one correspondence between a point in the parameter space $\boldsymbol{\theta}$ and the related fields of interest, $\boldsymbol{u}$, obtained from the solution of the physical problem (the disk plots in our case). The two different fidelity models used to investigate the behavior of the dual-rotor multicopter at different configuration are a CFD solver based model, and the blade element based RMAC

model. They are described next.

A. High-Fidelity Approach

CFD simulations are conducted using the commercial Navier-Stokes solver AcuSolve which uses a stabilized 2^{nd} order upwind finite element method. For a two-rotor unit, the computational domain is shown in Figure 1a, comprising of a rectangular prism with far-field boundary conditions on the front and top surfaces set to the freestream velocity. The sides, bottom and rear of the computational domain are set to outflow with backflow conditions enabled, which allows for flow in either direction across the boundary with zero pressure offset. All boundaries of the computational domain are at least 25 rotor radii away from the center of the aircraft in all directions. As indicated in Figure 1a, the computational domain consists of two rotating volumes (for the two-rotor unit) where the mesh inside the volume rotates along with the rotor geometry. Each rotating volume is a cylinder with radius 1.06 rotor radii. The height of the cylinder extends two tip chord lengths above and below the rotor plane. Each rotating volume is bounded by a sliding mesh interface which passes information into and out of the non-rotating volume that comprises the remainder of the computational domain.

The domain was discretized using a mesh comprised entirely of unstructured tetrahedral elements. Within both rotating volumes, the blade surface mesh was set to ensure 200 elements around the airfoil. The elements on the blade were refined by a factor of 10x near the leading (0-10% chord) and trailing edge (90-100% chord), compared to the elements along the remainder of the chord. The boundary layer in the wall normal direction is highly resolved, with the first element height set to ensure $y^+ < 1$. A refinement region, with element size prescribed as ½ tip chord is established for the off-body area around the rotors, and extends 0.3R above the rotor plane, and 1.5R below Figure 1b, with the mesh refinement below the rotor plane skewed towards the rear to better capture the rotor wakes as they convect downstream. The entire computational domain is comprised of 122 million elements, with 33 million in each rotating volume, and 56 million in the nonrotating volume. A mesh refinement study was performed in which the surface mesh size, edge refinement, boundary layer, and wake refinement were doubled independently. The results of the refinement study indicated that the thrust and torque changed by less than 1.5% and 2.5% respectively when compared to the original mesh (which is used for simulations in this study).

A detached eddy simulation (DES) is used with the Spalart-Allmaras (SA) turbulence model. All simulations were run initially using time steps corresponding to 10° of rotation for several revolutions to reduce computational cost of the rotor wake development. Each simulation was then restarted for additional revolutions at 1° time steps until convergence was achieved. The initial 10° time steps are possible without causing numerical divergence due to the stability afforded by the Streamline Upwind Petrov-Galerkin (SUPG) stabilized finite element method and Generalized a implicit time integration method. The latter method was designed to suppress high frequency distrubances and allow solution stability with Courant-Friedrichs-Lewy (CFL) number greater than 1 [19] [20]. All runs were performed on 512 2.6 GHz Intel Xeon E5 -2650 processors, part of the Center for Computational Innovations (CCI) at Rensselaer Polytechnic Institute.

B. Low-Fidelity Approach

The low-fidelity model used in this study is the Rensselaer Multicopter Analysis Code (RMAC, [18]). Blade element theory is used to calculate the lift and drag at a differential blade element. In the RMAC simulations presented, the blade is divided into 48 radial segments. Repeating the lift and drag calculations at each element yields a radial load distribution, which can be integrated to determine the individual blade loads. This can be performed for multiple azimuthal angles to produce a lift and drag distribution over the entire rotor disk.

A helical vortex-wake model is applied [21] to calculate the flow induced by the rotor. In this model, the rotor wake is represented by a vortex trailed from the tip of each rotor blade. As the rotor turns, the trailed vortices form filaments, which are convected downward by the mean rotor induced flow and backward by the free-stream velocity. By using the Biot-Savart law, the vortex-induced flow can be calculated at any point in space, which makes it capable of predicting rotor-rotor interference effects. For the simulations presented, the maximum wake age is 1440°, with a 2° resolution, resulting in 180 distinct azimuthal locations for the rotor lift and drag distributions.

C. Multi-Fidelity Approach

The high- and low-fidelity versions of the fields of interest are denoted by $\boldsymbol{u}^H(\boldsymbol{\theta})$ and $\boldsymbol{u}^L(\boldsymbol{\theta})$, respectively with $\boldsymbol{\theta} = (d_x, d_y)$. In this section we describe the method used to combine the these two models in order to construct a multifidelity approximation of the rotors disk plots at N points in the parameter space, $\tilde{\boldsymbol{u}}_i^H = \tilde{\boldsymbol{u}}^H(\boldsymbol{\theta}_i)$ with $i = 1, \ldots, N$,

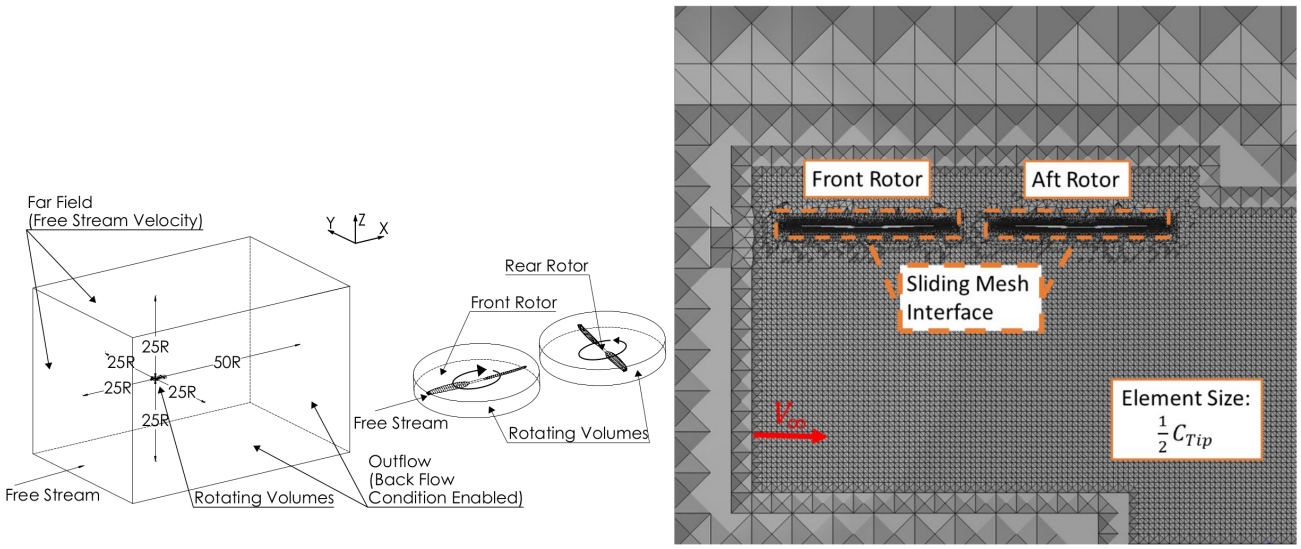

(a) Diagram of the computational domain **(b) Cross-section of wake mesh refinement**

Fig. 1 CFD simulation domain and mesh

while computing just $n \ll N$ high-fidelity simulation $\boldsymbol{u}_j^H$, $j = j(i)$, $i = 1, \ldots, n$. The number n is dictated by our computational budget, and the integer array $j(i)$ contains the list of "important" points in the parameter space. In order to find these important points, we use the low-fidelity model to investigate the parameter space.

In particular:

- **Step 1.** Perform N of simulations at the points $\{\boldsymbol{\theta}_i\}_{i=1}^N$ with the low-fidelity model, $\{\boldsymbol{u}_i^L\}_{i=1}^N$;
- **Step 2.** Find the $n \ll N$ most "important" snapshots $\boldsymbol{u}_{j(i)}^L$, $i = 1, \ldots, n$, and store the associated parameters points $\boldsymbol{\theta}_{j(i)}$;
- **Step 3.** Perform high-fidelity simulations $\left\{\boldsymbol{u}_{j(i)}^H\right\}_{i=1}^n$ just at these locations $\boldsymbol{\theta}_{j(i)}$, $i = 1, \ldots, n$;
- **Step 4.** Reconstruct the high-fidelity solutions $\left\{\tilde{\boldsymbol{u}}_i^H\right\}_{i=1}^N$ at all points $\{\boldsymbol{\theta}_i\}_{i=1}^N$ through a *lifting procedure*.

Below we describe these steps in more details.

Step 1 Once the N points in the parameter space are chosen, $\{\boldsymbol{\theta}_i\}_{i=1}^N$, e.g. by uniformly discretizing the domain of interest, the N low-fidelity simulations are performed at the these points, $\{\boldsymbol{u}_i^L\}_{i=1}^N$, and stored as columns of the matrix $\boldsymbol{U}^L = [\boldsymbol{u}_1^L, \ldots, \boldsymbol{u}_N^L]$.

Step 2 Thereafter, we perform a *pivoted QR decomposition* $\boldsymbol{U}^L\boldsymbol{P} = \boldsymbol{Q}\boldsymbol{R}$ to generate a permutation matrix $\boldsymbol{P}$, such that when applied to $\boldsymbol{U}^L$, the columns of $\boldsymbol{U}^L\boldsymbol{P}$ are ordered from the most important to the least. This order reveals the index array $j(i)$, $i = 1, \ldots, n$. It can be shown that among all the basis of n snapshots, the one formed by *those* n "important" snapshots $\boldsymbol{u}_{j(i)}^L$, associated with the points $\boldsymbol{\theta}_{j(i)}$, is the basis that minimizes the average l_2 error when the low-fidelity solutions are expressed in that basis.

We store the n snapshots $\boldsymbol{u}_{j(i)}^L$ in the matrix $\boldsymbol{U}_n^L$. Then, the least-square approximation of the low-fidelity solution at the i-th parameter value, $\boldsymbol{u}_i^L$, can be expressed using this basis as $\hat{\boldsymbol{u}}_i^L = \boldsymbol{U}_n^L\boldsymbol{c}_i$. The coefficients of this expansion are determined by solving the small, $n \times n$, linear system $\boldsymbol{G}\boldsymbol{c}_i = \boldsymbol{f}_i$, with $\boldsymbol{G} = (\boldsymbol{U}_n^L)^T\boldsymbol{U}_n^L$ being the Gramian matrix and $\boldsymbol{f}_i = (\boldsymbol{U}_n^L)^T\boldsymbol{u}_i^L$.

Step 3 The n high-fidelity simulations are performed at the points $\boldsymbol{\theta}_{j(i)}$, $i = 1, \ldots, n$, and the resulting snapshots $\boldsymbol{u}_{j(i)}^H$ are stored in the matrix $\boldsymbol{U}_n^H = [\boldsymbol{u}_{j(1)}^H, \ldots, \boldsymbol{u}_{j(n)}^H]$.

Step 4 The last step, called the *lifting procedure*, uses the snapshots computed in Step 3 as a basis, and the projection coefficients obtained in Step 2 to write an approximation of the high-fidelity snapshots at all the N locations $\{\boldsymbol{\theta}_i\}_{i=1}^{N}$ in the parameter space: $\hat{\boldsymbol{u}}_i^H = \boldsymbol{U}_n^H \boldsymbol{c}_i$, with $i = 1, \ldots, N$.

A graphical summary of the algorithm main concept is shown in Figure 2.

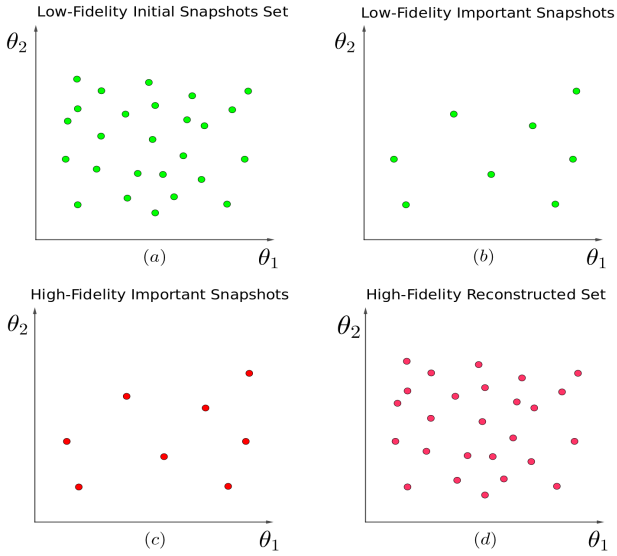

Fig. 2 Summary of the the proposed algorithm: (a) start with a low-fidelity set of snapshots, (b) select the most significant ones, (c) perform high-fidelity simulations at these points, (d) reconstruct the high-fidelity set using the coefficients computed with the low-fidelity set.

The approach described above is similar to Proper Orthogonal Decomposition (POD), which is also often used to identify an optimal basis. However, the critical difference is that in the method described above the optimal basis is formed by the snapshots themselves, whereas in POD each basis vector comprises of a linear combination of all snapshots. This means that with POD, an economical lifting procedure is not feasible.

Finally, we consider a slightly modified version of the proposed approach, applicable when N low-fidelity and n high-fidelity snapshots have already been computed. The set of n parameters values where the high-fidelity solutions are available can be pre-selected as the "important" parameters set. We can then apply steps 2 and 4 to construct the multi-fidelity solution at any other of the N values of the parameters. In the following section we use the multi-fidelity approach in this context.

IV. Numerical Results

The rotorcraft considered for this study has two identical counter-rotating rotors aligned with the longitudinal axis, where the front rotor rotates clockwise and the rear rotor counter-clockwise. The rotors have a radius of 0.8382m (33in) and the blades, whose plan form is shown in Figure 3, have a root pitch of 24° and linear twist rate of -12°. The forward speed is set to 20.58m/s (40 kts), and the rotor advance ratio, $\mu = 0.108$ for all the simulations [5].

As mentioned above, the parameters of the problem are the longitudinal and vertical distance between the rotors, denoted respectively as d_x and d_y. The region of investigation in the parameter space, which defines the different configurations of the rotorcraft under analysis, is given by the rectangle $d_x \in [2.25R,\ 4R]$ and $d_y \in [0,\ 0.75R]$.

In order to apply the multi-fidelity algorithm, $N = 105$ low-fidelity snapshots are obtained using RMAC by uniformly sampling over the parameter domain. In addition, 9 high-fidelity CFD simulations at the parameter values $(d_x, d_y) \in \{2.5R, 3R, 3.5R\} \times \{0, 0.25R, 0.5R\}$ are available.

Out of the 9 high-fidelity snapshots, we select the $n = 4$ corresponding to $(d_x, d_y) \in \{2.5R, 3.5R\} \times \{0, 0.5R\}$ (i.e. the corners) as the snapshots that we assume are known. We refer to these as our training set, since this basis is used to train our model. The five remaining snapshots, collectively referred to as the validation set, are used to estimate the

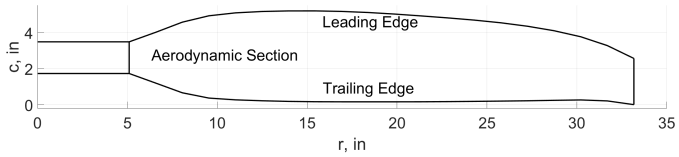

Fig. 3 Rotors blade planform, reproduced from [5]

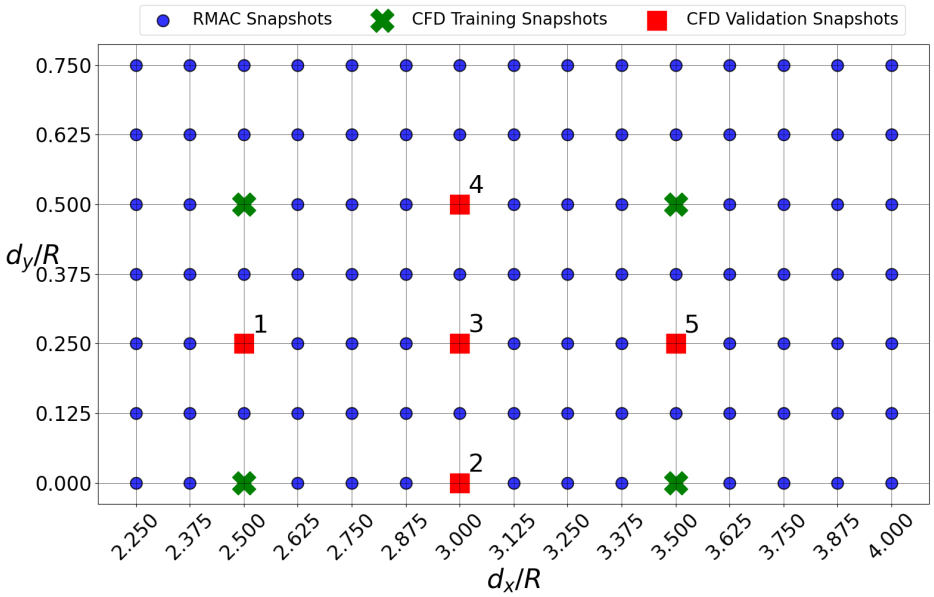

Fig. 4 High- and Low-Fidelity simulations in the parameter space. The High-Fidelity snapshots used as training set are indicated in green, and the ones for validation are colored in red.

error in the surrogate model generated from the training set. Each validation point is assigned a number, as shown in Fig. 4, which shows the (d_x, d_y) values taken for each simulation.

We begin with the low-fidelity snapshots obtained from the RMAC simulations. We project every low-fidelity snapshot on the subspace formed by the span of low-fidelity snapshots selected at the parameter values corresponding to the training set. We denote these approximations by as $\hat{\boldsymbol{u}}_i^L$. Thereafter, we compute the l_2 norm of the difference between these approximations and the actual low-fidelity snapshots over the entire parameter space. This provides us with a measure of the appropriateness of the chosen basis to represent the low-fidelity solution. This difference norm is plotted in Figure 5 for the cases when lift and drag disk plots are used as snapshots. We observe that the error is small (less than 2%), and goes to zero at the 4 locations that are used as the basis, and grows as we move away from them.

Next we apply the lifting procedure. This implies retaining the coefficients of the low-fidelity projections, and replacing the low-fidelity basis vectors with their high-fidelity counterparts. This allows us to construct the lifted high-fidelity approximation of the snapshots in the entire parameter space. These are denoted by $\hat{\boldsymbol{u}}_i^H$ and represent the main result of our algorithm.

We test the performance of our algorithm by comparing these lifted snapshots with the high-fidelity solutions from the validation set. The lift and drag results for the validation snapshot number 3 (see Fig. 4) are presented in Figs. 6 and 7, respectively.

Figure 6a shows the two rotors' lift distribution for CFD (top), RMAC (middle), and the multi-fidelity (bottom). As expected, all three models predict high lift on the advancing side of the rotors, with some bias toward the front of the rotors. Compared to the CFD solutions, the RMAC clearly exaggerates the tip losses, as well as the negative lift in the

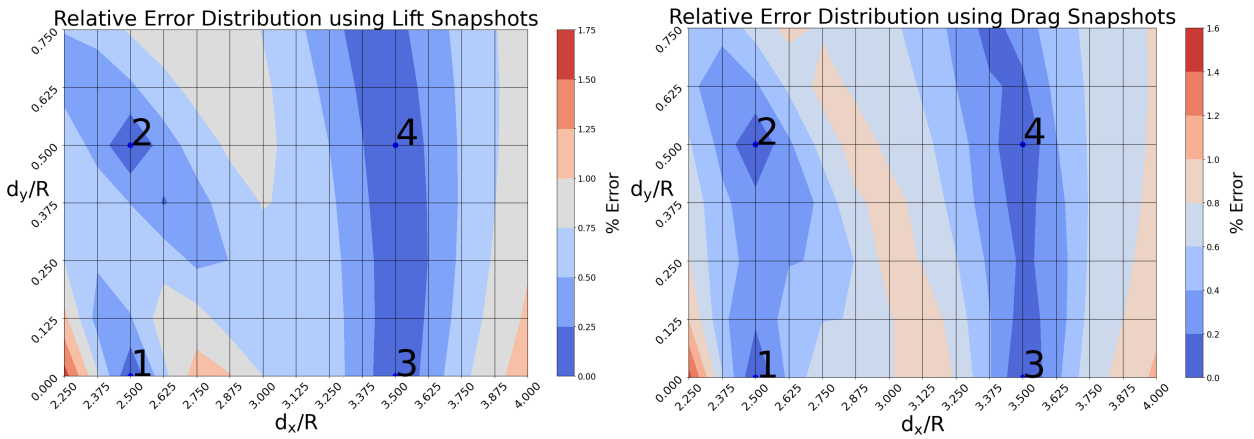

(a) Error in the lift disk plots. **(b) Error in the grad disk plots.**

Fig. 5 Distribution of error in the parameter space using the $n = 4$ dimension basis.

reverse-flow region for both rotors. Comparing the front and rear rotors, aside from a reflection about the 0°-180° line (due to the different spin directions), there is a large loss of lift on the front of the rear disk clearly visible in the CFD and multi-fidelity solutions due to the impingement of the front rotor's wake on the rear rotor. This effect is present, though less pronounced, on the RMAC simulations as well.

Fig. 6b shows the difference between the RMAC and multi-fidelity predictions and CFD. The prediction of lift distribution of the multi-fidelity model is significantly better than the RMAC prediction, which has significant error, especially in the tip region, where the tip-vortex is strongest.

Figure 7a shows similar results for the drag distribution on the rotor disk. Once again, the accuracy of the multi-fidelity model (as shown in Fig. 7b) is substantially better than the low-fidelity model. As was the case in lift, the

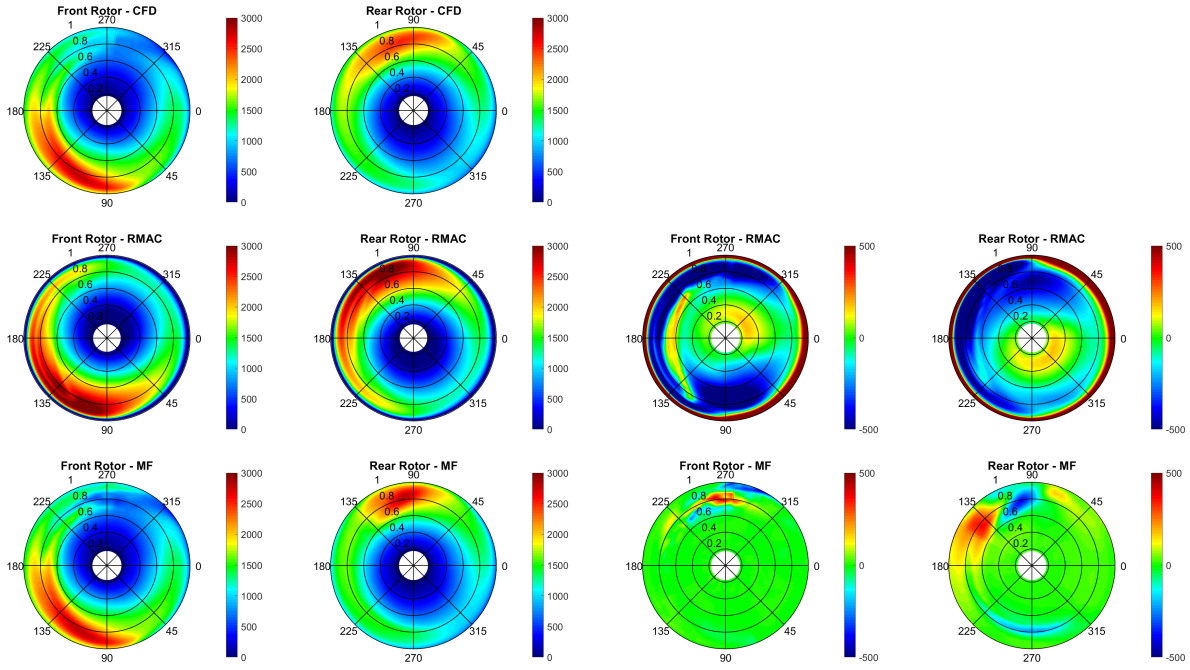

(a) Lift disk plots for the three methods **(b) Error in the RMAC and Multi-Fidelity lift disk plots**

Fig. 6 Low- and Multi-Fidelity lift disk plots. (Units N/m)

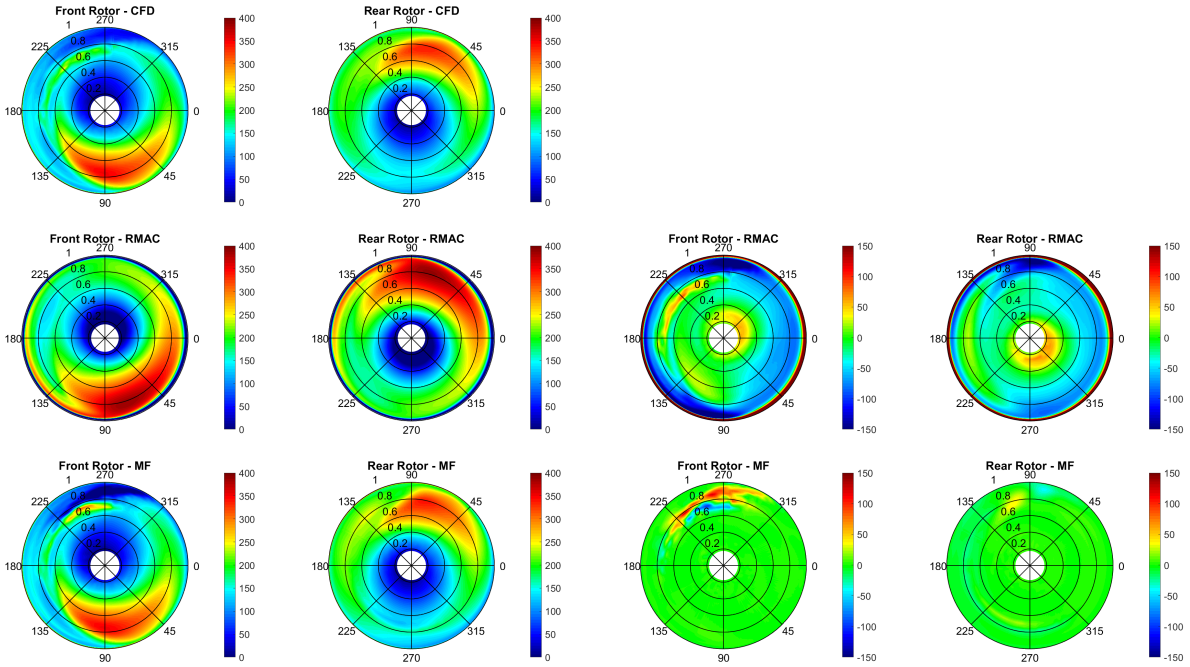

(a) Drag disk plots for the three methods **(b) Error in the RMAC and Multi-Fidelity drag disk plots**

Fig. 7 Low- and Multi-Fidelity drag disk plots (Units N/m).

error in the RMAC predictions is primarily on the tip of the blade, where the tip-vortex is most influential.

The accuracy of the distribution is quantified by Eq. 1, which is the ratio of the error between the lift (or drag) distribution predicted by a model (either RMAC or the multi-fidelity model) and the CFD prediction (taken to be the truth), normalized by the l_2 norm of the CFD-predicted load distribution. Multiplying by 100 results in "scores" for both models, with lower scores representing a distribution that better matches the CFD. The raw scores for lift and drag are tabulated in Tables 1 and 2, respectively. As expected, the multi-fidelity model has much better scores than the low-fidelity model. The error in RMAC is largely driven by the outboard 5% of the rotor, where tip vortex causes large negative lift. If this segment is ignored, the scores reduce signifcantly, though they are still higher than the multi-fidelity model.

$$S_i = 100 \times \frac{||\boldsymbol{u}_i^L - \boldsymbol{u}_i^H||}{||\boldsymbol{u}_i^H||} \tag{1}$$

Also of interest is the relative ability of these two models to predict the integrated rotor loads, such as thrust or torque, which are plotted for both models in Fig. 8. The broad trends of the front-rotor's thrust (Fig. 8a) are similar for both the low- and multi-fidelity models, showing a strong sensitivity to longitudinal proximity, and little sensitivity to vertical spacing. The dominant effect is due to the rear rotor's tip vortex inducing upwash on the front rotor, which is more powerful as the rotors get closer.

Table 1 Relative l_2 norm error in RMAC and multi-fidelity models in lift distribution.

Lift	Validation 1		Validation 2		Validation 3		Validation 4		Validation 5	
	Front	Rear	Front	Rear	Front	Rear	Front	Rear	Front	Rear
RMAC	77.46	82.01	76.85	82.67	79.29	81.55	79.02	81.15	79.04	82.28
RMAC*	19.64	22.58	18.42	25.34	21.29	22.71	20.38	21.99	20.79	24.66
MF	4.44	4.83	10.82	6.97	4.89	7.20	4.85	6.46	2.22	3.95

*Ignoring the outboard 5%

Table 2 Relative l_2 norm error in RMAC and multi-fidelity models in drag distribution.

Drag	Validation 1		Validation 2		Validation 3		Validation 4		Validation 5	
	Front	Rear	Front	Rear	Front	Rear	Front	Rear	Front	Rear
RMAC	123.1	118.3	125.0	116.4	123.7	118.2	122.9	119.7	123.2	117.1
RMAC*	28.76	25.04	28.71	21.60	30.64	24.17	30.02	25.62	30.21	22.42
MF	12.92	3.34	21.81	8.19	8.42	4.31	8.52	4.83	5.69	4.01

*Ignoring the outboard 5%

The opposite effect is observed on the rear rotor (Fig. 8c), where longitudinal spacing tends to decrease the lift produced. This is due to the front rotor waking down onto the rear rotor, an effect that is stronger as the rotors get closer together. There is also significant sensitivity to vertical spacing for rotors that are close longitudinally, and as the rear rotor is lifted above the front rotor, the thrust is generally increased. Both models predict much more sensitivity in the rear rotors' thrust to the rotor spacing than the front rotor, as expected from the wake convection.

Comparing the models to one another, RMAC overpredicts the thrust, relative to the CFD or multi-fidelity models, and the difference is largely uniform across d_x and d_y. Additionally, the multi-fidelity model also includes some curvature, visible between d_x = 2.75 and d_x = 3.5 that is not predicted by RMAC. Broadly speaking we observe that the multi-fidelity model uses the CFD solution in order to adjust the RMAC surface to a value that is more accurate.

The aerodynamic torque predictions for the front and rear rotor are plotted in Figs. 8b and 8d, respectively. Though the broad trends of decreasing rear-rotor torque with increasing vertical and longitudinal spacing are consistent between the low- and multi-fidelity models, there is a much more complex surface in the multi-fidelity model. On the front rotor, however, the trends are markedly different. The influence of the rear rotor on the front-rotor's torque is negligible in the RMAC model, due to the fact that the wakes move primarily downstream. However, the multi-fidelity model predicts a reduction in front-rotor torque at moderate separations, which is not captured by the low-fidelity model whatsoever.

The relative errors of the thrust and torque at the five validation points are tabulated in Tables 3 and 4, respectively. Broadly, the lower scores in the lift and drag distribution achieved by the multi-fidelity model correlate to better predictions of the rotor loads, though RMAC is capable of predicting both quantities within 8% in the worst-case. It is worth noting that the low-torque region on the front rotor (which validation point 2 is within) represents the largest torque error for RMAC, and is much more closely approximated by the multi-fidelity model, suggesting that the low-torque region predicted by the multi-fidelity model is not an aberration or numerical artifact, but is representative of a real phenomenon.

Table 3 Error in thrust computed using RMAC and multi-fidelity models.

Thrust [%]	Validation 1		Validation 2		Validation 3		Validation 4		Validation 5	
	Front	Rear	Front	Rear	Front	Rear	Front	Rear	Front	Rear
RMAC	1.98	1.07	1.53	7.42	3.34	3.94	2.37	3.16	2.42	4.96
MF	0.79	0.70	1.37	0.57	0.32	1.84	0.54	2.07	0.09	0.61

Table 4 Error in torque computed using RMAC and multi-fidelity models.

Torque [%]	Validation 1		Validation 2		Validation 3		Validation 4		Validation 5	
	Front	Rear	Front	Rear	Front	Rear	Front	Rear	Front	Rear
RMAC	6.61	1.96	7.42	1.20	6.02	1.92	4.37	3.32	4.13	0.95
MF	1.45	1.56	1.91	1.34	1.22	1.09	1.49	1.59	0.30	0.36

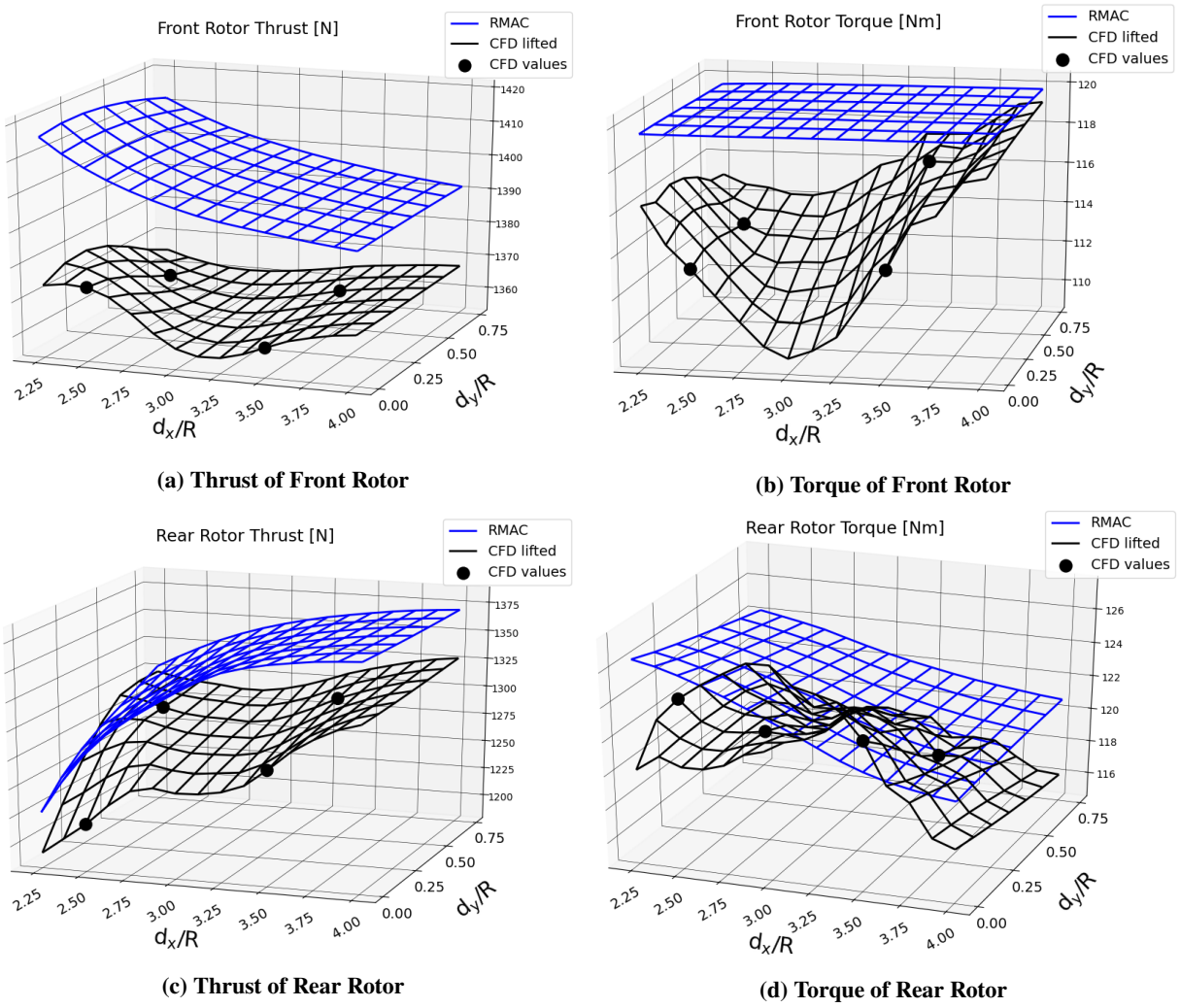

(a) Thrust of Front Rotor

(b) Torque of Front Rotor

(c) Thrust of Rear Rotor

(d) Torque of Rear Rotor

Fig. 8 Low- and Multi-Fidelity Thrust and Torque distribution over the parameter space

V. Conclusions

In this paper we have described a multi-fidelity approach for predicting lift and drag distributions in a multi-rotor rotorcraft. This approach combines the results from a low-fidelity, low-cost model, which is used to span the entire parameter space, with that of a high-fidelity, high-cost model, which is used to perform a few select simulations. In the example presented in this work, the low-fidelity model is a blade-element solver and the high-fidelity model is a CFD solver. We have demonstrated how the results from these very different models can be combined to produce multi-fidelity results that are much more accurate than the low-fidelity model, and much cheaper than the high-fidelity model by themselves. The trend of the rotors thrust and torque over the parameter space is better captured, with the multi-fidelity surrogate model showing more complex responses than the low-fidelity one. Predictions of the thrust and torque also improves, keeping the relative error under 2%. Future work in this direction involves using the proposed approach to select the important values of parameters at which to perform CFD simulation. Another interesting avenue of research is to extend this approach to a hierarchy of models: CFD with a fine mesh, CFD on a coarse mesh and RMAC and judiciously selecting the number of simulations at each level in order to obtain accurate simulations within a prescribed computational budget.

VI. Acknowledgements

This work is carried out at the Rensselaer Polytechnic Institute under the Army/Navy/NASA Vertical Lift Research Center of Excellence (VLRCOE) Program, grant number W911W61120012, with Dr. Mahendra Bhagwat as Technical Monitor

References

[1] S. Yoon, H. C. L., and Pulliam, T. H., "Computational Analysis of Multi-Rotor Flows," *International Journal for Numerical Methods in Engineering*, 2016.

[2] S. Yoon, D. D. B. J. W. M. C., P. V. Diaz, and Theodore, C. R., "Computational aerodynamic modeling of small quadcopter vehicles," *Proceedings of the 73rd Annual Forum, (Fort Worth), AHS International*, , No. 119, 2017, p. 567–589.

[3] Diaz, P. V., and Yoon, S., "High-Fidelity Computational Aerodynamics of Multi-Rotor Unmanned Aerial Vehicles," *AIAA SciTech Forum, American Institute of Aeronautics and Astronautics*, 2018.

[4] M. Misiorowski, F. G., and Oberai, A. A., "Computational study on rotor interactional effects for a quadcopter in edgewise flight," *AIAA Journal*, 2019. https://doi.org/https://doi.org/10.2514/1.J058369.

[5] R. Healy, M. M., and Gandhi, F., "A Systematic CFD-Based Examination of Rotor-Rotor Separation Effects on Interactional Aerodynamics for Large eVTOL Aircraft," 2019.

[6] A. Narayan, C. G., and Xiu, D., "A stochastic collocation algorithm with multifidelity models," *SIAM Journal of Computing*, 2014, pp. 2005–2035.

[7] X. Zhu, D. X., Akil Narayan, "Computational Aspects of Stochastic Collocation with Multifidelity Models," *SIAM/ASA Journal on Uncertainty Quantification*, 2014, pp. 444–463.

[8] J. Hampton, A. N. A. D., H. R. Fairbanks, "Practical error bounds for a non-intrusive bi-fidelity approach to parametric/stochastic model reduction," *Journal of Computational Physics*, Vol. 368, 2018, pp. 315–332.

[9] V. Keshavarzzadeh, R. M. K., and Narayan, A., "Parametric topology optimization with multiresolution finite element models," *International Journal for Numerical Methods in Engineering*, , No. 119, 2019, p. 567–589. https://doi.org/10.1002/nme.6063.

[10] Daniel J. Perry, A. N. R. T. W., Robert M. Kirby, "Allocation strategies for high fidelity models in the multifidelity regime," *SIAM/ASA Journal on Uncertainty Quantification*, 2019, pp. 203–231.

[11] D. Papailiopoulos, A. K., and Boutsidis, C., "Provable deterministic leverage score sampling," *Proceedings of the 20th ACM SIGKDD international conference on Knowledge discovery and data mining*, 2014, pp. 997–1006.

[12] C. Boutsidis, P. D., and Magdon-Ismail, M., "Near-optimal column-based matrix reconstruction," *SIAM Journal on Computing*, 2014, pp. 1–27.

[13] Chan, T. F., "Rank Revealing QR Factorization," *Linear Algebra Appl.*, 1987, pp. 67–82.

[14] Chan, T. F., and Hansen, P. C., "Some applications of the rank revealing QR factorization," *SIAM Journal on Scientific Computing*, 1992, pp. 727–741.

[15] Gu, M., and Eisenstat, S. C., "Efficient Algorithms for Computing a Strong Rank-Revealing QR Factorization," *SIAM Journal on Scientific Computing*, 1996, pp. 848–869.

[16] Chan, T. F., "Alternative to the SVD: Rank Revealing QR-Factorization," *SPIE Proceedings*, 1986.

[17] Y. P. Hong, C.-T. P., "Rank-Revealing QR Factorizations and the Singular Value Decomposition," *Mathematics of Computation*, , No. 197, 1992, pp. 213–232.

[18] Niemiec, R., and Gandhi, F., "Development and Validation of the Rensselaer Multicopter Analysis Code (RMAC): A Physics-Based Comprehensive Modeling Tool," *Vertical Flight Society*, 2019.

[19] K. E. Jansen, C. H. W., and Hulbert, G. M., "AA generalized-alpha method for integrating the filtered Navier-Stokes equations with a stabilized finite element method," 2000.

[20] Brooks, A. N., and Hughes, T. J., "Streamline Upwind/Petrov-Galerkin Formulations for Convection Dominated Flows with Particular Emphasis on the Incompressible Navier-Stokes Equations," *Computer Methods in Applied Mechanics and Engineering*, 1982, p. 199–259. https://doi.org/10.1002/nme.6063.

[21] Leishman, J. G., "Rotor Wakes and Tip Vortices," 2006, p. 567—654.